Renewable Energy 186 (2022) 691–703

Contents lists available at ScienceDirect

Renewable Energy

journal homepage: www.elsevier.com/locate/renene

A deep learning-based strategy for fault detection and isolation in parabolic-trough collectors

Sara Ruiz-Moreno *, Adolfo J. Sanchez , Antonio J. Gallego , Eduardo F. Camacho

Dept. de Ingeniería de Sistemas y Automática, University of Seville, Camino de los Descubrimientos, no number E-41 092, Seville, Spain

ARTICLE INFO

Article history:
Received 1 September 2021
Received in revised form
7 January 2022
Accepted 9 January 2022
Available online 13 January 2022

Keywords:
Solar energy
Parabolic-trough collectors
Artificial intelligence
Fault detection
Fault diagnosis

ABSTRACT

Solar plants are exposed to the appearance of faults in some of their components, as they are vulnerable to the action of external agents (wind, rain, dust, birds …) and internal defects. However, it is necessary to ensure a satisfactory operation when these factors affect the plant. Fault detection and diagnosis methods are essential to detecting and locating the faults, maintaining efficiency and safety in the plant. This work proposes a methodology for detecting and isolating faults in parabolic-trough plants. It is based on a three-layer methodology composed of a neural network to obtain a preliminary detection and classification between three types of fault, a second stage analyzing the flow rate dynamics, and a third stage defocusing the first collector to analyze thermal losses. The methodology has been applied by simulation to a model of the ACUREX plant, which was located at the Plataforma Solar de Almería. The confusion matrices have been obtained, with accuracies over 80% when using the three layers in a hierarchical structure. By forcing all the three layers, the accuracies exceed 90%.

1. Introduction

The most abundant source of energy on the Earth is solar energy [1]. This fact, coupled with the growing awareness of the impact of traditional energy sources emitting CO_2 to the atmosphere, has led to a great deal of interest in researching and promoting solar energy [2]. Within the different techniques for obtaining solar energy, this paper focuses on concentrating solar power (CSP), specifically on parabolic trough collector (PTC) fields, one of the two dominant CSP technologies. It has the advantage of being able to store the heated fluid to generate electricity in the absence of sunlight [3]. PTC plants are composed of collectors with a parabolic shape that reflects the solar energy onto a pipe located at their focal line. At the inside of the pipe, there is a heat transfer fluid (HTF) —usually synthetic oil or water— that absorbs the thermal energy from the sun to produce steam that drives a turbine generator.

Over the years, it has become increasingly possible to equip systems with a wide variety of sensors, actuators and other components that allow them to work with better performance. As a result, the possibility of one of these elements failing is increasing. Working with incorrect measurements and defective actuators can lead to incorrect plant behavior, low power output and dangerous situations. Systems capable of recognizing faults are needed to avoid these risky situations and that is where fault detection and diagnosis (FDD) techniques appear [4]. Fault detection determines fault occurrence by analyzing dependencies between measurable signals and triggering alarms when necessary. Fault diagnosis is divided into fault isolation, which determines the location of the fault, and fault identification, which determines the size of the fault. This paper focuses on fault detection and isolation of three types of faults in parabolic trough collectors. Fault-tolerant control (FTC) is the type of control that compensates the faults. Some works find that including an FDD module in a plant before FTC is a good step to help the control system and state that modularity makes them flexible and easy to implement [5].

Traditionally, most of the research in fault detection was directed to nuclear plants, aircraft, process plants, the automobile industry and national defense. Now, its use has been extended to many industries [4], being one of the most commons its application to DC motors. Isermann [6] collected some applications of FDD to DC motor drives, where parity equations and parameters estimation are combined. Other applications propose the use of constrained zonotopes for set-bases state estimators and fault detection [7] or address fault detection in a brushless motor using a particle filter as an observer [8]. In the field of energy systems,

* Corresponding author.
E-mail addresses: srmoreno@us.es (S. Ruiz-Moreno), asanchezdelpozo@us.es (A.J. Sanchez), agallego2@us.es (A.J. Gallego), efcamacho@us.es (E.F. Camacho).

https://doi.org/10.1016/j.renene.2022.01.029

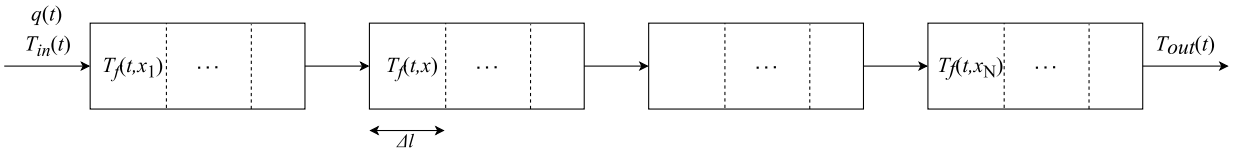

Fig. 1. Schematic of one loop of the collector field. $T_{in}(t)$ and $T_{out}(t)$ are the inlet and outlet temperatures, $T_f(t, x)$ is the fluid temperature and $q(t)$ is the flow rate.

Table 1
Parameters and variables description.

Symbol	Description	Units
$\rho(t, T)$	Density	kg/m^3
$C(t, T)$	Specific heat capacity	J/(kg °C)
A	Cross-sectional Area	m^2
$T(t, x)$	Temperature	°C
t	Time	s
x	Space	m
$I(t)$	Direct solar irradiance	W/m^2
K_{opt}	Optical efficiency	–
$n_o(t)$	Geometric efficiency	–
G	Collector aperture	m
$H_l(t, T)$	Thermal loss coefficient	W/(m^2 °C)
$T_a(t)$	Ambient temperature	°C
L	Length of the inner circumference of the pipe	m
$H_t(t, T)$	Metal-fluid heat transmission coefficient	W/(m^2 °C)
$q(t)$	Flow rate	l/s
L_{loop}	Loop length	m
A_f	Transversal area of the interior pipe	m^2
S	Total area of the field	m^2

Marquez et al. [9] applied a fault detection and reconfiguration method to the energy management system of a microgrid. It was based on obtaining residuals to extract fault information and send it to a reconfiguration block. Applications of fault detection, estimation and fault-tolerant control in the context of microgrids can be found in the survey by Morato et al. [10]. Ruiming et al. [11] proposed a method to identify early defects of wind turbines using a dynamical network marker as warning signal with data of SCADA. Regarding the application of fault detection to photovoltaic systems, Hussain et al. [12] used radial basis functions with two input parameters.

In the field of solar energy, most of the applications are related to fault detection in solar thermal systems rather than fault diagnosis in solar power plants. In some recent works [13,14], different deep learning models are trained to predict the performance of solar hot water systems under different meteorological conditions and detect faults whenever the predictions and measurements are too far apart from each other. The approach proposed by de Keizer et al. [15] simulated a solar thermal system and then compared the measured and simulated energy yields to detect faults. Wiese et al. [16] carried out simulations in solar heating systems to form a confidence interval of the solar gain to detect faults. Heuristic rules are used by Sun et al. [17] to perform fault diagnosis in solar heating systems. The work carried out by de Keizer et al. [18] analyzed methods to determine simulation uncertainties and obtain better residuals in solar thermal systems. Neural networks are used by He et al. [19] to detect faults and classify them by level of severity in solar hot water systems. Faure et al. [20] presented a methodology to determine the detectable faults in a collector and apply it to opacification. A method combining support vector machines and D-S evidence theory is presented by Jiang et al. [21] to detect and classify four types of faults in solar water heaters.

Regarding fault diagnosis to solar thermal power plants and, specifically, to parabolic-trough collectors, there are few applications in the literature. They mainly base on isolating between areas of the solar field, considering the collector zone as a whole subsystem instead of distinguishing between different parts of the collectors. Kalogirou et al. [22] implemented FDD in a solar thermal plant by using four neural networks to predict four temperatures in different locations of the plant. With those predictions, they obtained residuals to detect faults and determine if it is located in the collectors or the pipes between the collectors and the storing system. A similar simplification is made by Zahra et al. [23], who use fuzzy sliding mode observers for detecting faults considering the collectors as a closed subsystem. An application to parabolic-trough collectors was carried out by Cardoso et al. [24,25], where faults are detected by obtaining residuals from a model of the plant.

In this work, a three-layer methodology with artificial neural networks is proposed to detect and diagnose faults in parabolic-trough collectors, addressing the challenge of distinguishing between types of failures in these plants. The difficulty is because the different types of failures are closely coupled, and it is not straightforward to isolate the errors.The main contributions of this work are the use of artificial neural networks combined with a hierarchical decoupling strategy to detect and isolate faults in a PTC plant and the isolation of three types of faults inside the collectors area.

This novel approach can isolate faults in the optical efficiency of the collectors, the flow rate, and the thermal losses, which poses an advantage with respect to previous works in the field. Faults in the optical efficiency are related to reflectivity and associated with breakage, degradation, corrosion and coating of the collectors due to dirt or external elements, faults in the flow rate are related to an unbalance of the loop with respect to the entire plant —the flow rate assumed in a loop is the pump flow rate divided by the number of loops as done by Gallego et al. [26], assuming there is one flow meter for the entire plant located at the pump, as in most real plants—, and faults in thermal losses are related to dirt, wear, insulation and breakage of the pipes, associated with vacuum losses in the tubes. For example, a temperature drop could be due to a broken collector but also to a misreading of the flow rate in the loop or pipe breakage. It is necessary to distinguish where the failure has occurred to solve it quickly since the treatment is different in each case. Cleaning a dirty collector is cheap, but changing a flow meter is expensive, so it is desirable to do it only when it is certain that this is the defective component. With this method, the warnings obtained will allow the fault to be localized quickly and in a more individualized way than previous literature methods avoiding risks and energy losses associated with reflectivity drops and loss coefficient.

This paper is organized as follows. First, in section 2, a description of the model used and the control architecture is given. Section 3 gives a brief description of artificial neural networks. The proposed three-layer methodology is presented in section 4 and the modes of operation are described in section 5. The simulation results are presented in section 6 and finally, some discussion and conclusions are given in sections 7 and 8.

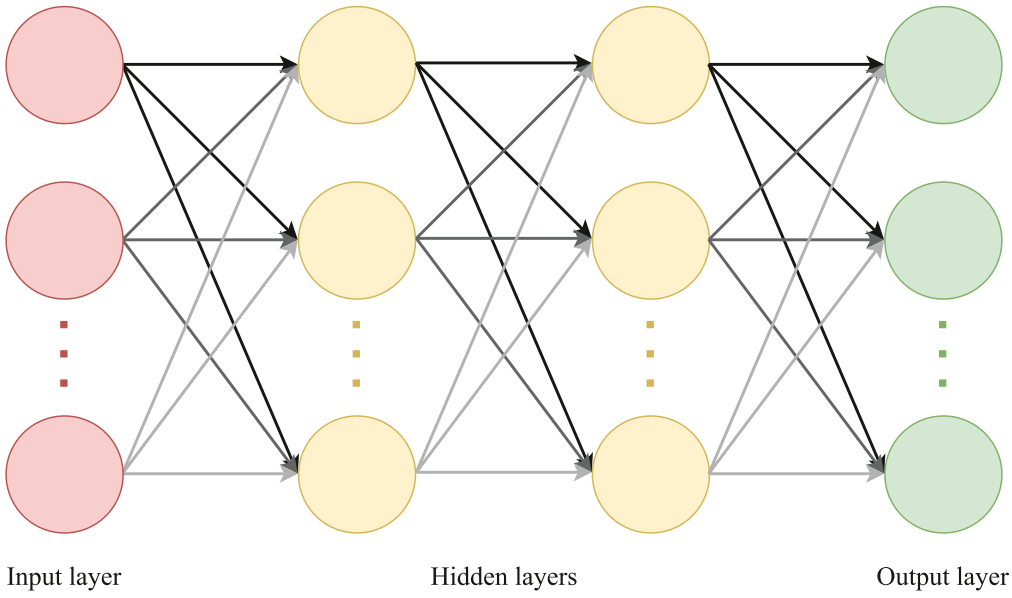

Fig. 2. Schematic of a multilayer perceptron.

2. Model of the parabolic trough collector

This section describes the ACUREX plant [27,28] used for simulation, the two models employed, and the control architecture. The plant has been widely used in the literature and was located at the Plataforma Solar de Almería, Spain. It consists of 10 loops of 4 parabolic-trough collectors with 12 modules, each of the loops with a length of 172 m and divided into segments of length $\Delta l = 1$ m. Each loop is conformed by an active and a passive part. The active part receives solar radiation and measures 142 m, while the passive part is not receiving solar radiation and measures 30 m. The HTF used is Therminol 55 thermal oil. In this work, one loop is considered, see Fig. 1, and the adaptation of the method to more loops is straightforward, applying the neural networks to each loop independently.

2.1. Distributed parameter model

The model used for simulation is the distributed parameter model (DPM) [27,29], which allows describing the system with spatially distributed variables. Equations (1) and (2) describe the energy balances on the metal and the fluid with the notation given by Table 1, where the subscript m refers to metal and f refers to fluid. The faults are modeled as multiplicators $\alpha_{K_{opt}}$ lower than 1, α_q greater or lower than one and α_{Hl} greater than one. Values of 1 mean no-fault.

$$\rho_m C_m A_m \frac{\partial T_m}{\partial t} = \alpha_{K_{opt}} I K_{opt} n_o G - \alpha_{Hl} H_l G (T_m - T_a) - L H_t (T_m - T_f) \tag{1}$$

$$\rho_f C_f A_f \frac{\partial T_f}{\partial t} + \alpha_q \rho_f C_f q \frac{\partial T_f}{\partial x} = L H_t (T_m - T_f) \tag{2}$$

The HTF (therminol 55) density ρ_f and specific heat capacity C_f are computed by equation (3).

$$\rho_f = 903 - 0.672 T_f \tag{3a}$$

$$C_f = 1820 - 3.478 T_f \tag{3b}$$

The metal-fluid transmission coefficient H_t and the thermal losses coefficient H_l are given by equations (4) and (5).

$$H_t = q^{0.8}\left(2.17 \cdot 10^6 - 5.01 \cdot 10^4 T_f + 4.53 \cdot 10^2 T_f^2 - 1.64 T_f^3 + 2.1 \cdot 10^{-3} T_f^4\right) \tag{4}$$

$$H_l = 0.002\,49\left(T_f - T_a\right) - 0.061\,33 \tag{5}$$

Two types of efficiency affecting radiation are described in the literature [30,31]. The geometric efficiency n_o, sometimes referred to as $cos(\theta)$, depends on the hourly angle, Julianne day, solar hour, declination, latitude, and collector dimensions [32]. It is determined by the position of the mirrors normal vector with respect to the radiation beam vector and can be computed online. The optical efficiency K_{opt} is a factor that takes into account reflectivity, tube absorptance, interception factor, mirror soiling and other losses. Normally, this factor is estimated and considered constant, but its value can vary due to multiple causes, such as dirt or deterioration of the mirrors or deterioration of the selective coating of the tubes.

2.2. Lumped parameter model

The lumped parameter model (LPM) or concentrated parameter model provides an approximation of the field without considering the metal-fluid heat transmission coefficient or the spatial distribution of temperatures. This model is used for implementing the controller and in the thermal losses fault detection, where the values of the multiplicators α are unknown and assumed equal to 1. It describes the variation in the internal energy of the fluid, given by equation (6).

$$C_{loop} \frac{dT_{out}}{dt} = \alpha_{K_{opt}} n_o K_{opt} S I - \alpha_q q P_{cp} (T_{out} - T_{in}) - \alpha_{Hl} H_l A (T_{mean} - T_a) \tag{6}$$

where $C_{loop} = \rho_m C_m A_f L_{loop}$ is the thermal capacity of the loop, $P_{cp} = \rho_m C_m$, the subscript *in* refers to inlet, *out* stands for outlet and T_{mean} is the mean temperature between the input and the output.

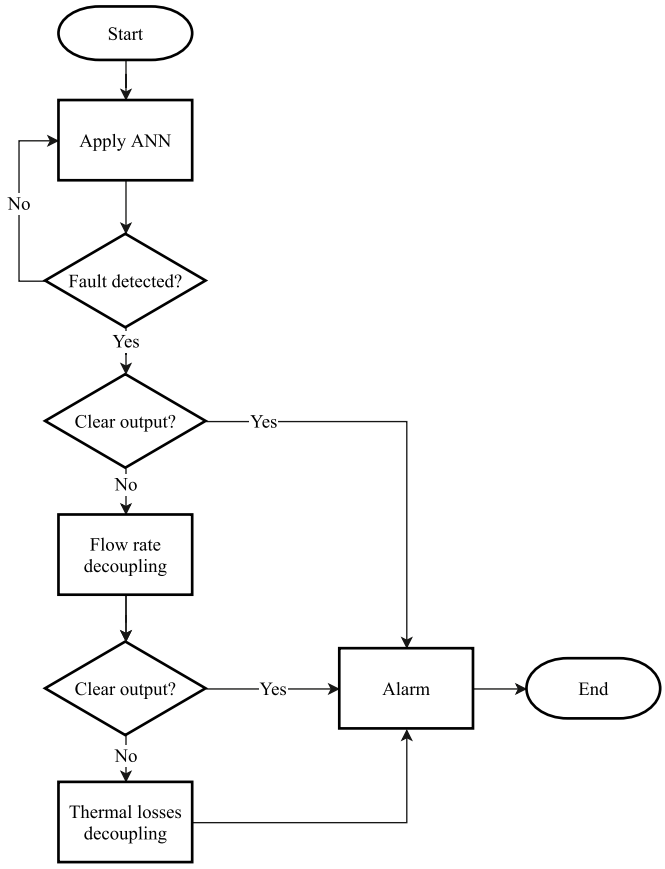

Fig. 3. Scheme of the three-layer methodology for decoupling faults in the collector optical efficiency, the flow rate, and the thermal losses.

2.3. LPM flow control

In this work, a simple controller is used for temperature reference T_{ref} tracking manipulating the flow rate $q(t)$. A series feedforward controller is implemented based on the LPM description given above to obtain the control signal as in equation (7). The controller sample time is 39 s, a typical sample time used in the literature [33,34]. It is appropriate for the dominant time constants of the ACUREX solar field when working at different regimes.

$$q(t) = \frac{n_o K_{opt} SI - H_l A(T_{mean} - T_a)}{P_{cp}(T_{ref} - T_{in})} \tag{7}$$

3. Artificial neural network

In this work, the output of a neural network will be used as the basis for fault detection in a solar collector. This section aims to briefly introduce artificial neural networks by describing their primary operating principle.

An artificial neural network (ANN) is a type of model that can approximate every nonlinear function by combining weighted sums of linear functions. They are distributed in a series of layers and nodes—also called neurons—that try to mimic the behavior of the human brain. ANNs originate from the work developed by McCulloch and Pitts [35], where the aim was to emulate a neural network using electrical circuits and, although their use was not very popular at the beginning due to the cost of training, recent technological advances have made them very widespread today.

One of the most known types of ANNs is the multilayer perceptron (MLP), whose scheme is shown in Fig. 2. It is a feedforward neural network, which means that the neurons in a layer are all connected to the neurons in the previous layer without cycles between them [36]. As shown in the figure, there are three types of layers in an MLP: the input and output layers, directly connected to the input and output data, and the hidden layers that transform the information. Each neuron of an ANN computes a linear regression problem and the combination of different neurons gives place to more complex functions. The output of each neuron is generally transformed to an active or non-active state by the use of activation functions that are, generally, relay, sigmoid or hyperbolic tangent.

The parameters (weights) of each neuron are the coefficients of a linear regressor and must be obtained during the training process. In neural networks with hidden layers, this is accomplished by the backpropagation algorithm [37]. This algorithm actualizes the weights of the neurons by using their gradients, according to the direction in which the cost function decreases fastest. The scaled conjugate gradient algorithm [38] is a type of conjugate gradient method, where a search is performed along conjugate directions to obtain a faster convergence. Before training the ANN, the dataset is generally divided into three subsets: training set (for adjusting the parameters), validation set (for validating the behavior and adjust parameters) and test set (for estimating the behavior of the ANN with new data). The process of selecting the neural network architecture (type of ANN, number of layers and number of neurons) is performed by trial and error until finding a neural network that performs well on the three subsets.

3.1. Evaluation metrics

Different metrics can be used to select one neural network over others. This work uses the percentage error and accuracy for selecting the neural networks and the confusion matrix, accuracy, and F1-score to validate the results. The F1-score is computed from precision and recall:

- Percentage error: given a vector of N outputs $z_i = [z_{i1}, z_{i2}, \ldots, z_{iN}]^T$, takes the index of the component with higher value. For each output i, ind is defined as:

$$ind(z_i) = \arg\min_j z_i j \tag{8}$$

Let z be the real outputs of the data and $\hat{z}$ the outputs of the ANN. Then, the percentage error Per is the proportion of instances i where $ind(z) \neq ind(\hat{z})$.

- Confusion matrix: It is a matrix that takes account of the number of instances of each class and the number of instances assigned to each class.
- Accuracy: the hit rate, being TP the number of true positives, TN the number of true negatives, FP the number of false positives and FN the number of false negatives.

$$Acc = \frac{TP + TN}{TP + TN + FP + FN} \tag{9}$$

- Precision: the rate of correct TP over all positive-assigned instances.

$$Pre = \frac{TP}{TP + FP} \tag{10}$$

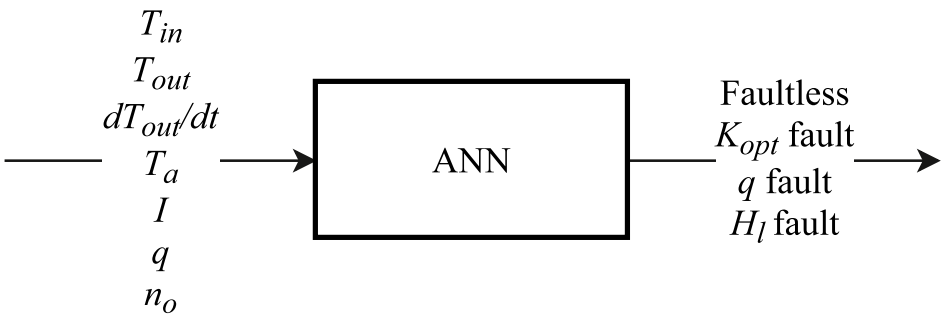

Fig. 4. Scheme of the artificial neural network, being T the temperature, I the irradiance, q the flow rate, n_o the geometric efficiency, K_{opt} the collector optical efficiency and H_l the thermal loss coefficient. The subscripts *in*, *out* and *a* refer to inlet, outlet and ambient, respectively.

Table 2
Results of the neural networks.

Neurons	Per (%)	Acc train (%)	Acc validation (%)	Acc test (%)
21	22.36	77.7	77.4	77.7
49	20.14	79.9	79.9	79.9
49–32	8.39	91.6	91.5	91.7
49-32-16	9.64	90.4	90.1	90.4
70-49-16	11.76	88.2	88.3	88.3
100	19.71	80.3	80.2	80.4

- Recall: the rate of correct TP over all positive instances.

$$Rec = \frac{TP}{TP + FN} \tag{11}$$

- F1-score: the harmonic mean of precision and recall.

$$F1 = 2 \cdot \frac{Pre \cdot Rec}{Pre + Rec} \tag{12}$$

4. Three-layer "hierarchical" methodology

A new method has been designed for detecting three types of faults in parabolic-trough collectors. Given a certain fault in the plant, the objective is to detect and distinguish between three types of fault: collector optical efficiency (mainly due to reflectivity), flow rate and thermal losses. Then, the corresponding alarm is activated. The proposed method is composed of three layers:

- Artificial Neural Network.
- Flow rate decoupling.
- Thermal losses decoupling.

This section aims to provide a complete description of the method, which is schematized in Fig. 3. This method uses an

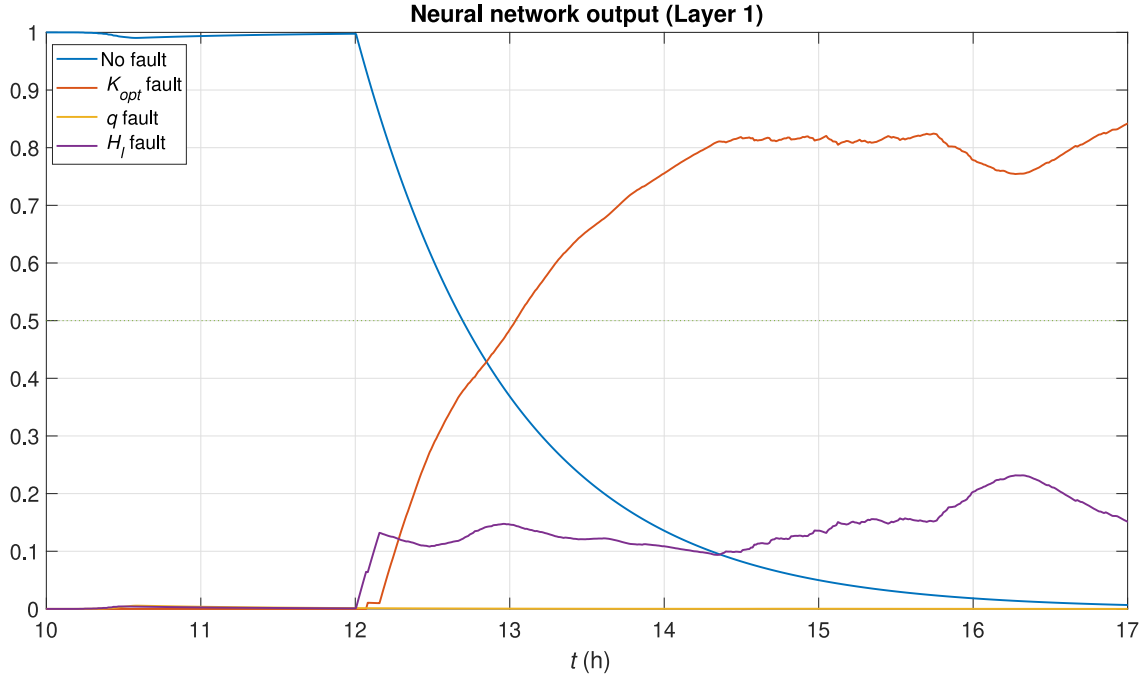

Fig. 5. Output of the neural network with a fault in K_{opt} of 10% at 12:00.

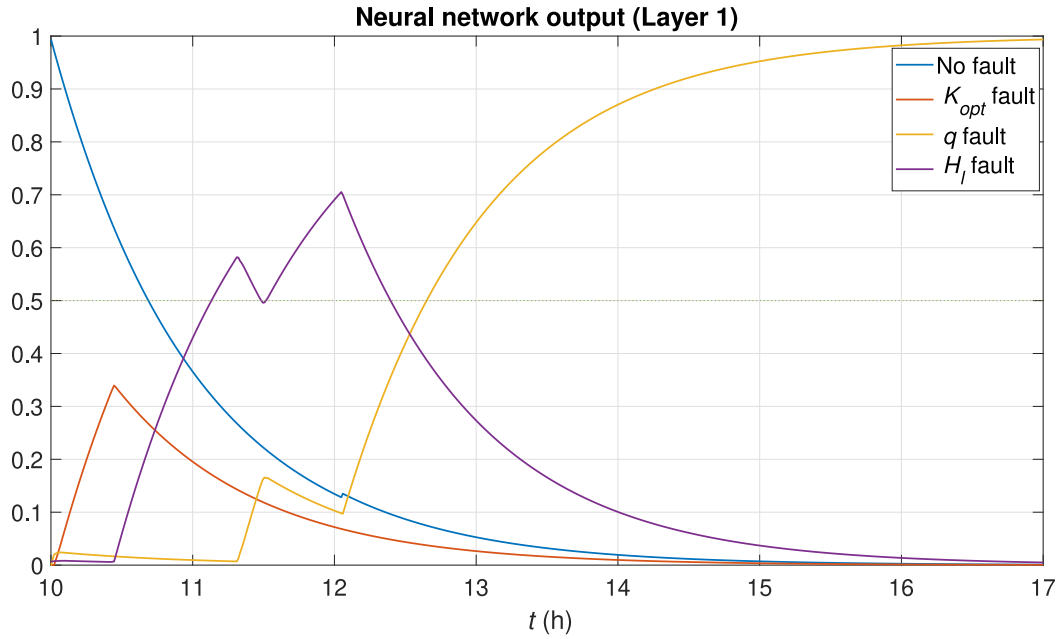

Fig. 6. Output of the neural network with a fault in q of −0.5 l/s at 10:00.

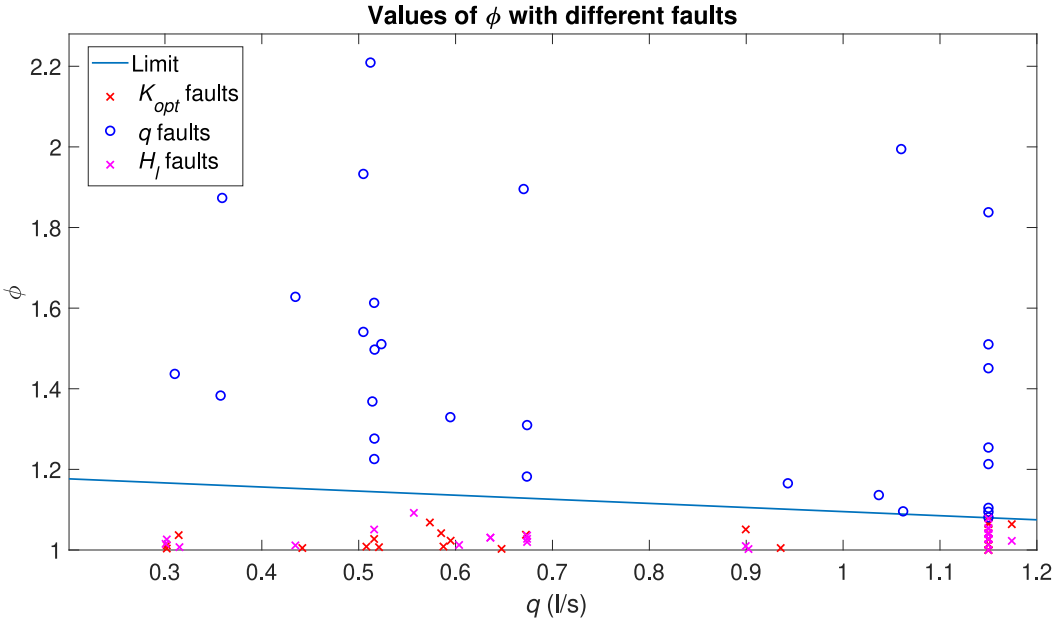

Fig. 7. Values of φ for different types of fault with a line to distinguish the flow faults.

artificial neural network as a preliminary detector of the fault, and then two stages of discrimination are used to decouple the types of faults and improve the results.

4.1. First layer: ANN

The first step is applying an Artificial Neural Network to detect the faults in the plant. One important step when applying neural networks is selecting the inputs, as data irrelevant to the output could slow down training and worsen the behavior. In this case, the previous knowledge of the system dynamics has been used and the same inputs used in the concentrated parameter model have been selected: the inlet and outlet temperature of the collector loop, the time derivative of the outlet temperature, the ambient temperature, the irradiance, the assumed flow rate and the optical efficiency. The outputs directly determine the existence of failures in the three locations contemplated. Therefore, the ANN has four outputs scaled between 0 and 1. These outputs are related to no-fault, fault in the optical efficiency K_{opt}, fault in the flow rate q and fault in the thermal loss coefficient H_l. A low value for one of these variables indicates a low likelihood of that situation, while high values indicate that this is likely to be the governing situation. Fig. 4 shows the scheme of the neural network.

Several simulations have been performed combining different

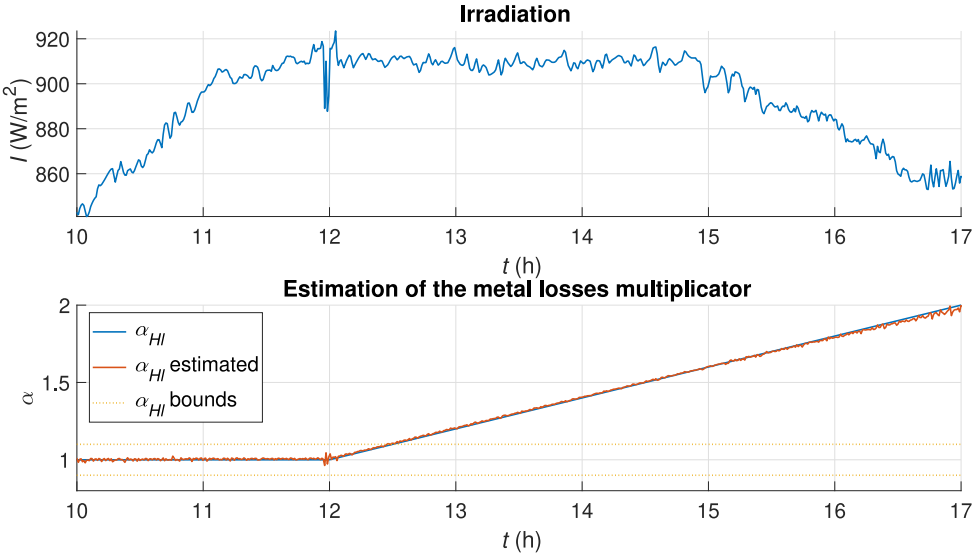

Fig. 8. α_{H_l} estimations obtained in a one-day simulation with a reference temperature of 250 °C.

irradiance values between 800 W/m^2 and 1000 W/m^2, reference temperatures between 210 °C and 300 °C and failure times between 10 h and 14 h. Lower values would hinder the operation due to a change in the dynamics of the plant. For this reason, the method is applied on clear days or situations with an stable operation where no passing clouds are affecting the field. A dataset of 1087 992 data was obtained, which was divided into training (75%), validation (10%) and test (15%) sets. Different ANNs have been trained with scaled conjugate gradient backpropagation. Table 2 shows the results obtained from these neural networks, indicating the number of nodes in each hidden layer in column "Neurons". The selected ANN is the third one, with 49 nodes in the first hidden layer and 32 in the second one, as it provides the lowest percentage error and the greatest accuracies. All layers contain hyperbolic tangent sigmoid functions, except for the last one, which contains a softmax function that transforms the data into the range [0,1].

Once selected, the neural network is applied to the plant with a sample time of 39 s, which is the same as the controller sample time. To avoid false alarms due to instantaneous changes in the plant, the output of the neural networks is filtered with a time constant of 1 h. Afterward, a failure will be detected when one of the outputs is greater than 0.5. The ANN is applied to one-day simulations with constant perturbances for a more straightforward visualization of the results. Fig. 5 shows the output of the neural network after a K_{opt} fault of 10% occurring at 12:00 with a reference temperature of 300 °C and a constant irradiance of 800 W/m^2. As it can be observed, before 12:00, the output of the neural network is "no-fault". When the fault appears, it can be seen how the neural network output starts to change. The output related to a fault in the optical efficiency increases reaching a high value, and the fault can be detected.

Sometimes, neural networks may give non-determinant results. As an example of these occasions, Fig. 6 shows a case of −0.5 l/s fault in the flaw rate at hour 12 with a reference temperature of 300 °C and a constant irradiance of 1000 W/m^2. This graph shows how the neural network detects a wrong fault during the first 2 h. This is because in this type of plant, the faults are very closely coupled to each other, and it can be very complicated to decouple them with a single model. The methodology proposed for decoupling the faults will be explained in the following sections of this document.

Table 3
Confusion matrix for mode 1.

		Real			
		faultless	K_{opt}	q	H_l
Predicted	faultless	**170**	0	13	0
	K_{opt}	38	**151**	13	5
	q	6	59	**143**	5
	H_l	2	6	47	**206**

Table 4
Confusion matrix for mode 2.

		Real			
		faultless	K_{opt}	q	H_l
Predicted	faultless	**174**	3	13	0
	K_{opt}	39	**197**	3	1
	q	1	13	**145**	2
	H_l	2	3	55	**213**

Table 5
Confusion matrix for mode 3.

		Real			
		faultless	K_{opt}	q	H_l
Predicted	faultless	**180**	0	13	0
	K_{opt}	36	**211**	9	9
	q	0	5	**194**	0
	H_l	0	0	0	**207**

Table 6
Accuracies and F1-scores of each mode.

Mode	F1-score (%)				Acc (%)
	Faultless	K_{opt} fault	q fault	H_l fault	
1	85.21	71.39	66.67	86.37	77.55
2	85.71	86.40	76.92	87.12	84.38
3	88.02	87.73	93.49	97.87	91.67

4.2. Second layer: flow rate decoupling

As the neural network sometimes encounters difficulties in alarming, a second layer is designed to decouple the flow-rate faults from the others when the output of the neural network is not completely clear. The strategy consists of imposing a small drop of 0.1 l/s and analyzing the dynamics of the system in the second collector, which will be different for scenarios with a fault in the flow rate, as it is the governing variable. Cases with faults in reflectivity or thermal losses should not affect significantly. If the rise time of the temperature t_s of 25% differs from a specific value, a flow-rate fault is detected. For this purpose, a small dataset of 231 data has been constructed to model the relationship between q, t_s and n_o. This dataset will be used to obtain a reference rise time t_s^0 by interpolation. Then, the residual φ is obtained:

$$\varphi = \max\left(\frac{t_s}{t_s^0}, \frac{t_s^0}{t_s}\right) \tag{13}$$

The limit of the residual must be lower for higher values of the flow rate. This is performed by using a variable limit given by $\varphi_{max} = -0.101\,695q + 1.196\,95$, experimentally obtained from the dataset. Some experiments have been carried out to validate this layer of the methodology. Fig. 7 shows the values of φ obtained by applying different types of faults to the plant, varying the moment and size of the fault.

It is worth mentioning the extreme situation in which the mirrors are completely dirty or broken since, in this case, the temperature will not be affected by a variation in the flow rate. If this occurs, a failure in the optical efficiency K_{opt} will be alarmed directly. If a variation in the temperature of the second collector is detected and the residual φ exceeds the limit, a flow-rate failure will be alarmed. Otherwise, faults in the flow rate are discarded, and the next layer can be applied.

4.3. Third layer: thermal losses decoupling

If the non-existence of flow-rate failures has been confirmed, it is possible to analyze the thermal losses. The strategy is to defocus the first collector of the loop and estimate the coefficient H_l from the lumped-parameter model of equation (6) applied to this collector. Defocusing is a mechanism that consists of reducing the global efficiency of a collector by modifying the angle of incidence of the sun's rays. This mechanism is used in commercial plants to avoid excessively high oil temperatures and has been included in the control strategy in Ref. [39]. It is possible to use the lumped-parameter model after decoupling the other two variables: the flow rate is known to be non-faulty and the effect of total defocusing causes the efficiency of the collectors to cease to affect the model, resulting in equation (14). An estimate of the multiplier α_{H_l} has been added to be used as a residual of the thermal losses to be extracted from equation (14).

$$C_{loop}\frac{\partial T_1}{\partial t} = -qP_{cp}(T_1 - T_{in}) - \hat{\alpha}_{H_l}H_l{\cdot}A(T_{mean,1} - T_a) \tag{14}$$

where T_1 is the temperature in the center of the first collector and $T_{mean,1}$ is the mean temperature between the input and the center of the first collector.

When the residual value is 10% away from unity —i.e., $\alpha_{H_l} \notin (0.9, 1)$—, it is considered that there is a failure in the thermal losses and so it will be alarmed. Fig. 8 shows the value of α_{H_l} obtained in a one-day simulation with a reference temperature of 250 °C and a variable irradiance profile where an incipient fault was introduced. The estimated value of α_{H_l} always stays close to the actual value and, during the non-failure time, it is far from the limits. Although there is a fair amount of slack in these limits, they help avoid false positives when sudden changes in irradiance occur, such as the one before hour 12.

5. Operating modes

The proposed methodology is composed of three phases, each one dedicated to decoupling one type of fault. As previously shown, the neural network is capable of detecting a high failure rate on its own, so it is possible to use it without activating the other two phases. On the other hand, the use of the three stages provides better fault detection at the cost of momentarily stopping the normal operation of the plant. According to the advantages and disadvantages of the three layers, the proposed method can be applied in three different modes:

1. Using only the first layer (ANN).
2. Using the three layers (as represented in Fig. 3).
3. Using the ANN only to distinguish between faulty/non-faulty and force the next two layers whenever a fault is detected, regardless of the type of fault that the ANN is alarming.

Since the neural network outputs must sum to 1, the first mode decides that failure has been detected when one of the outputs associated with failure is greater than 0.5. In this way, the fault is assigned to the output with the highest value and it is taken into account that the value of the output associated with no-fault is low.

Mode 2 is the standard mode, since it decides when each of the three phases needs to be applied. First, the output with the highest value is selected as a candidate and then checked to ensure that it is greater than 0.9. If not, the flow rate is checked. If the output associated with the flow rate is not too low—in this case, it has been selected to be greater than 0.2—, the flow rate is checked. If no flow

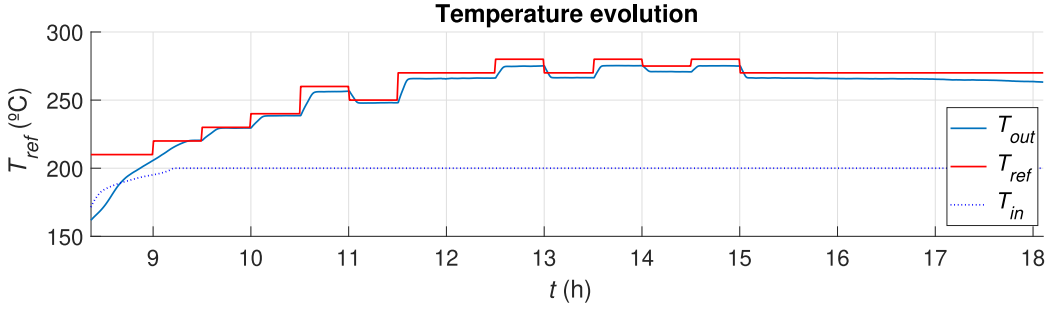

Fig. 9. Reference temperature profile.

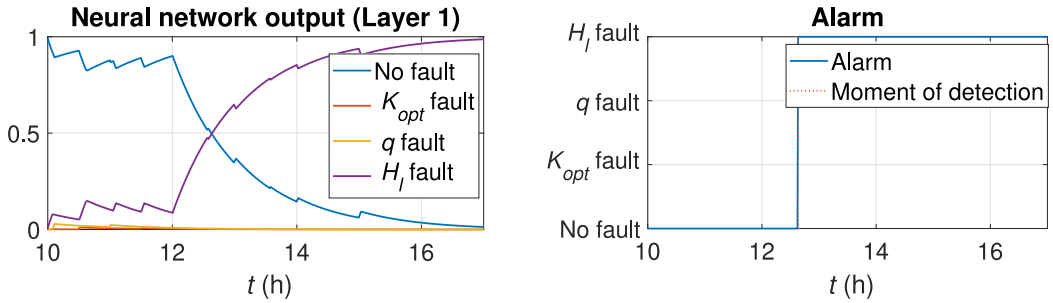

Fig. 10. Results for a 115% fault introduced in the thermal losses at 12:00.

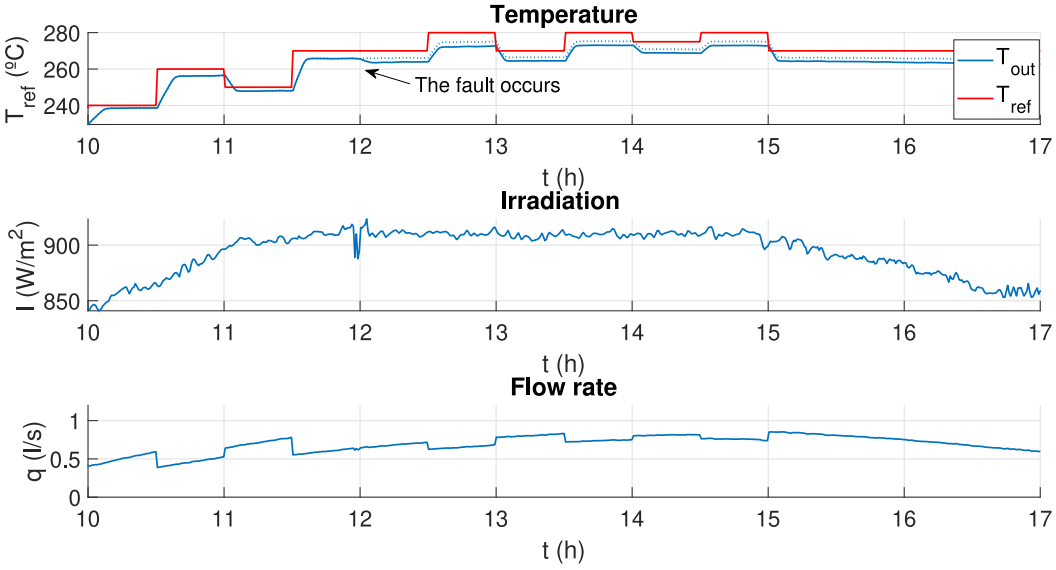

Fig. 11. Temperature, irradiation and flow rate for a 115% fault introduced in the thermal losses at 12:00. The discontinuous line shows the non-faulty temperature.

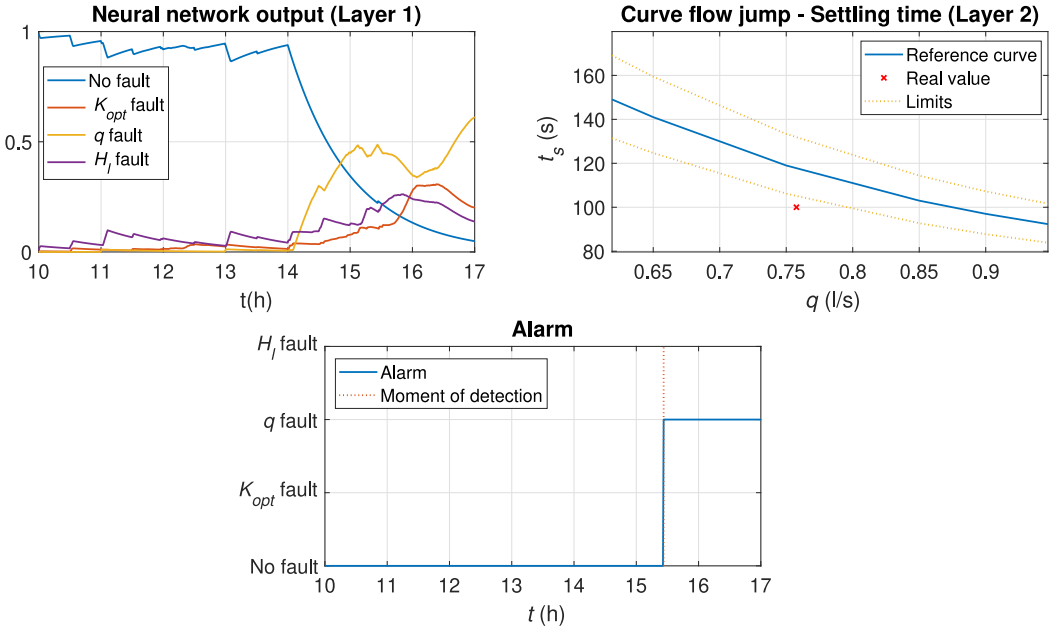

Fig. 12. Results for a +0.1 l/s in the flow-rate at 14:00.

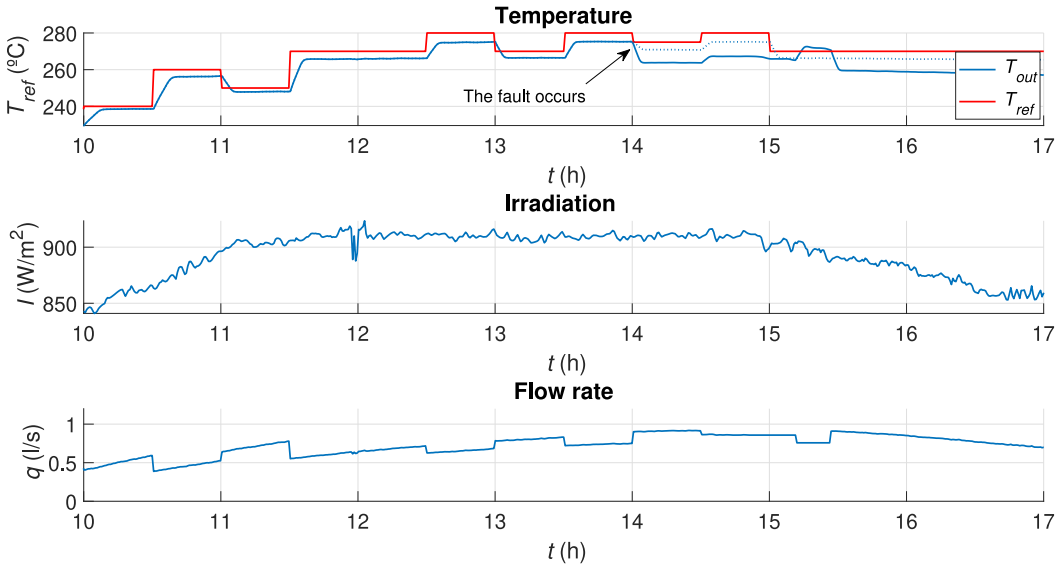

Fig. 13. Temperature, irradiation and flow rate for a +0.1 l/s in the flow-rate at 14:00. The discontinuous line shows the non-faulty temperature.

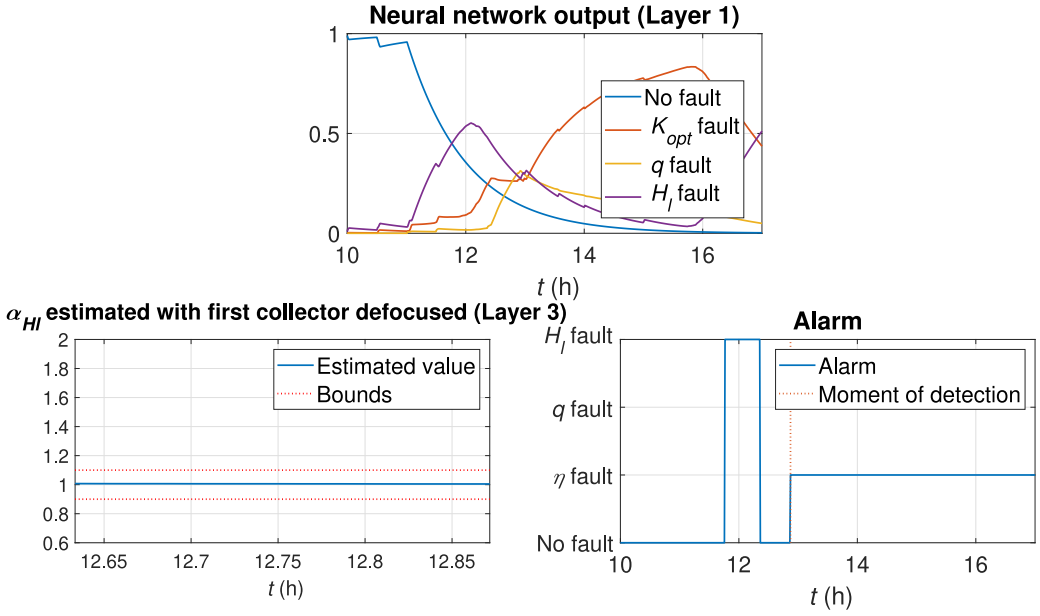

Fig. 14. Results for a 80% in the optical efficiency at 11:00.

failure is detected, the third stage is started as long as the output associated with the losses is at least twice the output associated with the optical efficiency.

Finally, mode 3 consists of applying the three stages, one after the other. The neural network is used only to distinguish between failure and non-failure. As soon as the output associated with non-fault is not the highest value, the flow decoupling stage is applied. If, after this stage, no flow failure is detected, it moves to the third stage, where it will be decided whether it is a failure in the optical efficiency or the losses.

To compare the three modes, one-day simulations have been carried out using constant parameter values, with irradiances between 800 and 1000 W/m^2 and reference temperatures between 210 and 300 °C. In each of these simulations, abrupt failures occurring at different times between hours 10 and 14 were simulated. Wide ranges of faults have been used to cover the different possibilities, with multiplicative faults in the optical efficiency between 10 and 90% (100% means no failure), additive faults in flow rate between −0.5 l slash s and +0.5 l slash s (0 means no failure), and multiplicative faults in thermal losses between 110 and 200%. The confusion matrices obtained with these simulations are given by Tables 3–5 and the accuracies and F1-scores are shown in Table 6.

6. Results

This section aims to provide some results obtained by simulating the complete system under different circumstances. In order to obtain results similar to real applications, variable values of irradiance and reference temperature have been used. Several tests

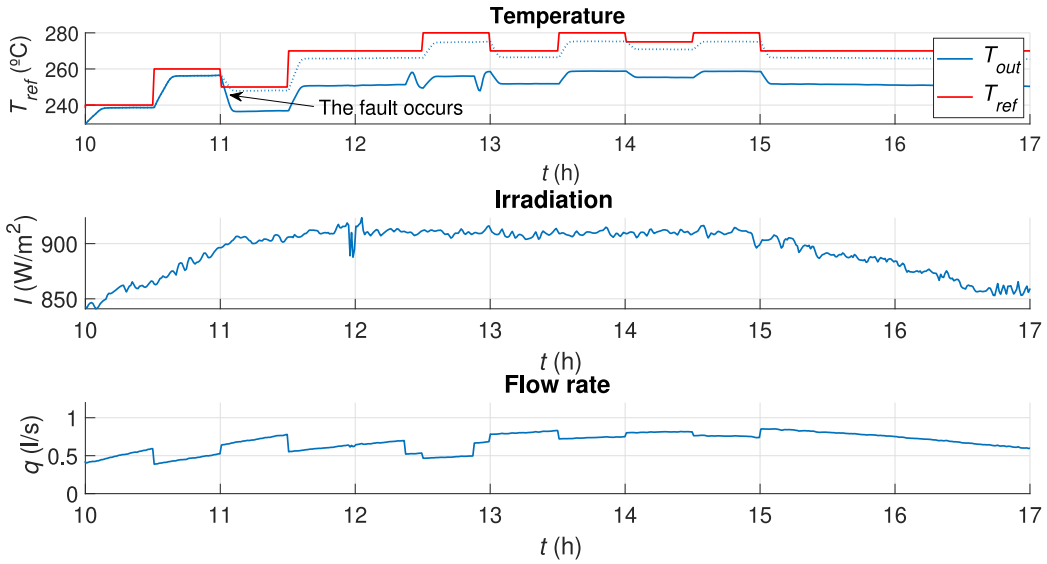

Fig. 15. Temperature, irradiation and flow rate for a 80% in the optical efficiency at 11:00. The discontinuous line shows the non-faulty temperature.

Table 7
Confusion matrix for mode 1 with a large neural network (ANN 2).

		Real			
		faultless	K_{opt}	q	H_l
Predicted	faultless	**216**	0	10	0
	K_{opt}	0	**185**	11	0
	q	0	29	**149**	9
	H_l	0	2	46	**207**

Table 8
Confusion matrix for mode 2 with a large neural network (ANN 2).

		Real			
		faultless	K_{opt}	q	H_l
Predicted	faultless	**216**	0	10	0
	K_{opt}	0	**196**	7	1
	q	0	20	**148**	6
	H_l	0	0	51	**209**

Table 9
Confusion matrix for mode 3 with a large neural network (ANN 2).

		Real			
		faultless	K_{opt}	q	H_l
Predicted	faultless	**216**	0	13	0
	K_{opt}	0	**213**	12	8
	q	0	3	**191**	1
	H_l	0	0	0	**207**

Table 10
Accuracy and F1-score for each mode with a large neural network (ANN 2).

Mode	F1-score (%)				Acc (%)
	Faultless	K_{opt} fault	q fault	H_l fault	
1	97.74	89.91	73.95	87.90	87.62
2	97.74	93.33	75.90	87.82	89.00
3	97.08	94.88	92.94	97.87	95.72

have been carried out using the irradiance and temperature set-points profiles shown in Figs. 8 and 9, respectively. These profiles have been applied for different types of faults using mode 2 since it provides a compromise between precision in the detection and performance of the plant.

In Fig. 10, a 115% fault was introduced in the thermal losses at 12:00. The output of the ANN was clear enough, with no need for the next layers of the strategy, so the system detects the fault precisely. The evolutions of the temperature, irradiance and flow rate are shown in Fig. 11, where a drop in the outlet temperature can be observed.

Fig. 12 shows the results obtained introducing a fault of $+0.1l$/s to the flow rate at 14:00. In this case, the second layer of the strategy was satisfactorily applied. The effect of the failure in the outlet temperature can be seen in Fig. 13. In this case, the drop is highly appreciable, as well as the effect of the decoupling strategy around 15:15.

Fig. 14 shows the results obtained with a multiplicative fault of 0.8 (drop of 20%) in the optical efficiency from 11:00, where the output was not clear too and the third layer helped distinguish between faults in the optical efficiency and thermal losses. Fig. 15 shows the evolution of temperature, irradiation and flow rate and compares the temperature obtained with the temperature that would be obtained in a non-faulty scenario. The huge difference makes it crucial to solve the failure.

Different neural networks can be used as first layer of the method. Tables 7–10 gather the confusion matrices, accuracies and F1-scores obtained using a neural network of 400 nodes in the first layer and 200 nodes in the second one. Since the number of correct outputs of the neural network is quite high and the errors correspond to wrong saturated outputs of the neural network, there is not much difference between the first two modes. The use of larger neural networks improves results at the expense of higher computational cost and longer training times.

7. Discussion

In this section, a discussion of the results obtained and the applicability of the proposed method is carried out. Some comments are extracted:

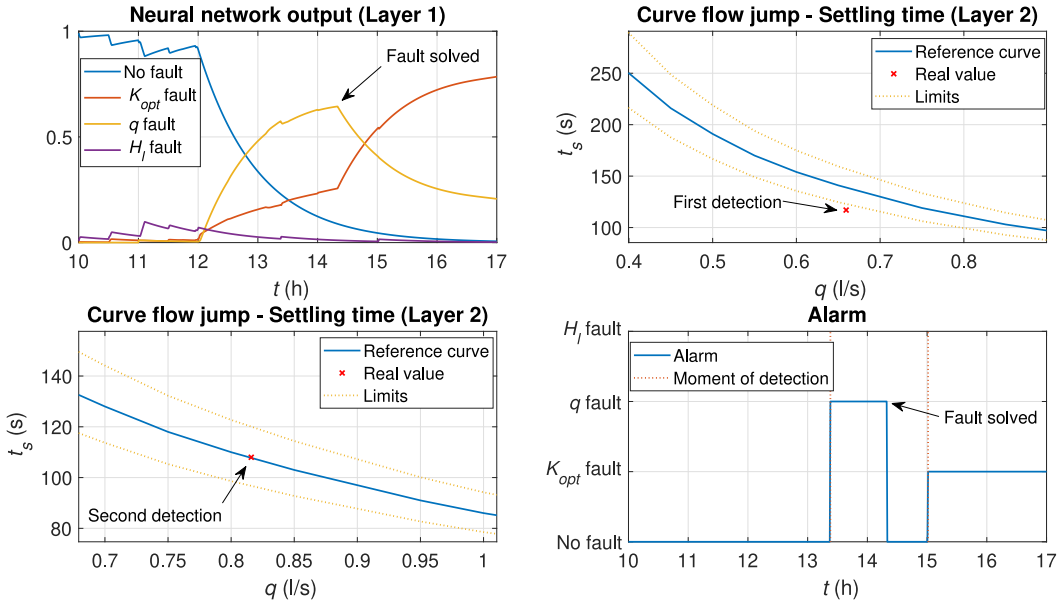

Fig. 16. Results for a 75% in the optical efficiency and a +0.15 l/s in the flow rate at 12:00.

- The second neural network requires a greater training effort and its use is limited to systems with sufficient computational capacity, but it provides better results, increasing the accuracy by 4.62%.
- The results are improved by applying failure decoupling stages. Mode three provides the highest accuracy at the expense of modifying the flow rate and defocusing the collectors each time a fault appears in the plant. In contrast, mode two obtains a lower accuracy, but modifications are only made to the plant behavior when deemed necessary. The selection of one method or the other will depend on the specific application and circumstances, and the choice is left to the operator.
- In an actual plant, the probability of more than one fault occurring simultaneously is very low. Even though the proposed methodology considers this circumstance implicitly and can even detect more than one fault on some occasions. The proposed system will detect one of the two failures and send the necessary information to the operators. When the corresponding fault is fixed, the system will alarm again, this time detecting the remaining fault. An example is shown in Fig. 16, where a multiplicative fault of 0.75 was introduced in the optical efficiency and an additive fault of 0.15 was introduced in the flow rate at 12:00. The system detects the fault in the flow rate and, when the operator solves it, the other fault is detected. A more exhaustive study of these cases will be the subject of future development.

8. Conclusions

In this work, a methodology is proposed for fault diagnosis in parabolic-trough plants. Three types of faults are detected and isolated: faults in the optical efficiency, the flow rate and the thermal losses. An artificial neural network is used to detect faults and obtain a first approximation of the fault classification. Then, two stages are added by slightly modifying the flow rate and the defocusing of the collectors to analyze the dynamics and improve the results. These stages are combined in a three-layer hierarchical methodology.

Three modes of operation have been proposed depending on the credibility given to the initial neural network and the importance given to the fault decoupling stages. The first mode only uses the ANN layer, the third mode always uses the other two layers, and the second mode is an intermediate approach between them. The more layers of decoupling types of faults are forced to act, the better the results, but at the expense of small disturbances in the normal operation of the plant.

Regarding the applicability of this method to an actual plant, real data could be used. The dataset of this work was obtained from 11787 h of simulation in one loop. Given that there is only enough radiation around 7 h a day, this dataset corresponds to 4.6 years with forced faults and fault-free. However, the ACUREX plant is formed by 10 loops, reducing the required time to 168 days. This number is decreased for commercial plants, from which past data is available. For instance, Solacor 2 [40] (with 90 loops) would need 19 days, and Mojave [41] (with 282 loops) would need 6 days. This calculation does not consider that obtaining the desired faulty data in real plants is not straightforward, so it would be necessary to augment the collected data and then apply techniques to reduce them selectively. A model of the plant could be adjusted to generate more days with cases that occur infrequently in a real plant and reduce the time required.

Future work will focus on using this methodology on the entire plant, analyzing the different faults on each collector and for all the loops in the plant, as well as improving the methodology in order to determine the magnitude of the failures and study the occurrence of multiple simultaneous faults.

CRediT authorship contribution statement

Sara Ruiz-Moreno: Conceptualization, Methodology, Software, Writing – original draft. **Adolfo J. Sanchez:** Conceptualization, Methodology, Software, Writing – review & editing. **Antonio J. Gallego:** Conceptualization, Methodology, Software, Writing – review & editing. **Eduardo F. Camacho:** Supervision, Writing – review & editing, Project administration, Funding acquisition.

Declaration of competing interest

The authors declare that they have no known competing financial interests or personal relationships that could have appeared to influence the work reported in this paper.

Acknowledgement

This research was supported by the European Union's Horizon 2020 research and innovation program under the ERC Advanced Grant agreement No 789 051.

References

[1] Z. Şen, Solar energy in progress and future research trends, Prog. Energy Combust. Sci. 30 (4) (2004) 367–416.
[2] M. Blanco, S. Miller, 1 - introduction to concentrating solar thermal (cst) technologies, in: M.J. Blanco, L.R. Santigosa (Eds.), Advances in Concentrating Solar Thermal Research and Technology, Woodhead Publishing Series in Energy, Woodhead Publishing, 2017, pp. 3–25.
[3] M.T. Islam, N. Huda, A.B. Abdullah, R. Saidur, A comprehensive review of state-of-the-art concentrating solar power (csp) technologies: current status and research trends, Renew. Sustain. Energy Rev. 91 (2018) 987–1018.
[4] D. Miljković, Fault detection methods: a literature survey, in: MIPRO, 2011 Proceedings of the 34th International Convention, 2011, pp. 750–755.
[5] E. Bernardi, E.J. Adam, Observer-based fault detection and diagnosis strategy for industrial processes, J. Franklin Inst. 357 (14) (2020) 10054–10081.
[6] R. Isermann, Fault-diagnosis Systems: an Introduction from Fault Detection to Fault Tolerance, Springer Science & Business Media, 2006.
[7] J.K. Scott, D.M. Raimondo, G.R. Marseglia, R.D. Braatz, Constrained zonotopes: a new tool for set-based estimation and fault detection, Automatica 69 (2016) 126–136.
[8] L.M.S. Vianna, J.P.S. Gonçalves, F. Fruett, M. Giesbrecht, Fault detection in brushless dc motor via particle filter, in: 2020 IEEE 29th International Symposium on Industrial Electronics, ISIE, 2020, pp. 295–299.
[9] J. Marquez, A. Zafra-Cabeza, C. Bordons, M.A. Ridao, A fault detection and reconfiguration approach for mpc-based energy management in an experimental microgrid, Control Eng. Pract. 107 (2021) 104695.
[10] M.M. Morato, P.R.C. Mendes, J.E. Normey-Rico, Dealing with energy-generation faults to improve the resilience of microgrids: a survey, in: 2019 IEEE PES Innovative Smart Grid Technologies Conference - Latin America, ISGT Latin America, 2019, pp. 1–6.
[11] F. Ruiming, W. Minling, G. xinhua, S. Rongyan, S. Pengfei, Identifying early defects of wind turbine based on scada data and dynamical network marker, Renew. Energy 154 (2020) 625–635.
[12] M. Hussain, M. Dhimish, S. Titarenko, P. Mather, Artificial neural network based photovoltaic fault detection algorithm integrating two bi-directional input parameters, Renew. Energy 155 (2020) 1272–1292.
[13] C. Correa-Jullian, J.M. Cardemil, E.L. Droguett, M. Behzad, Assessment of deep learning algorithms for fault diagnosis in solar thermal systems, in: ISES Solar World Congress 2019, 2019.
[14] C. Correa-Jullian, J.M. Cardemil, E. López Droguett, M. Behzad, Assessment of deep learning techniques for prognosis of solar thermal systems, Renew. Energy 145 (2020) 2178–2191.
[15] C. de Keizer, S. Kuethe, U. Jordan, K. Vajen, Simulation-based long-term fault detection for solar thermal systems, Sol. Energy 93 (2013) 109–120.
[16] F. Wiese, K. Vajen, M. Krause, A. Knoch, Automatic fault detection for big solar heating systems, in: Proceedings of ISES World Congress 2007, I–Vol. V, Springer, 2008, pp. 759–763.
[17] C.K. Sun, C.W. Chan, P. Tontiwachwuthikul, Intelligent diagnostic system for a solar heating system, Expert Syst. Appl. 16 (2) (1999) 157–171.
[18] A. de Keizer, K. Vajen, U.-k. Jordan, Sensitivity and uncertainty analysis for fault detection in solar thermal systems, in: Proc. Of Solar World Congress, vol. 28, Kassel, 2011.
[19] H. He, D. Menicucci, T. Caudell, A. Mammoli, Real-time fault detection for solar hot water systems using adaptive resonance theory neural networks, Energy Sustainability 54686 (2011) 1059–1065.
[20] G. Faure, M. Vallée, T. Tran-Quoc, N. Lamaison, C. Paulus, A Methodology to Analyse Fault Effect on Large Solar Thermal System Behaviour, 2018.
[21] S. Jiang, M. Lian, C. Lu, S. Ruan, Z. Wang, B. Chen, SVM-DS fusion based soft fault detection and diagnosis in solar water heaters, Energy Explor. Exploit. 37 (3) (2019) 1125–1146.
[22] S. Kalogirou, S. Lalot, G. Florides, B. Desmet, Development of a neural network-based fault diagnostic system for solar thermal applications, Sol. Energy 82 (2) (2008) 164–172.
[23] T. Zahra, L. M. Mourad, A. H. Ahmed, Robust fuzzy sliding mode observer for faults detection in solar power plant application., Instrum. Mes. Métrol. 19 (4).
[24] A. Cardoso, P. Gil, J. Henriques, P. de Carvalho, H. Duarte-Ramos, A. Dourado, A Robust Fault Tolerant Control Framework: Application to a Solar Power Plant, 2003.
[25] A. Cardoso, P. Gil, J. Henriques, P.d. Carvalho, H. Duarte-Ramos, A. Dourado, Experiments with a fault tolerant adaptive controller on a solar power plant, in: CONTROLO04, 6th Portuguese Conf. On Automatic Control, Faro, Portugal, Citeseer, 2004.
[26] A.J. Gallego, M. Macías, F. de Castilla, E.F. Camacho, Mathematical modeling of the Mojave solar plants, Energies 12 (21) (2019) 4197.
[27] E.F. Camacho, M. Berenguel, F.R. Rubio, Advanced Control of Solar Plants, Springer, 1997.
[28] E.F. Camacho, M. Berenguel, F.R. Rubio, D. Martinez, Control of Solar Energy Systems, Springer-Verlag, 2012.
[29] R. Carmona, Analisis, modelado y control de un campo de colectores solares distribuidos con sistema de seguimiento en un eje, Universidad de Sevilla, Seville.
[30] D.Y. Goswami, F. Kreith, J.F. Kreider, Principles of Solar Engineering, CRC Press, 2000.
[31] R. Österholm, J. Pålsson, Dynamic modelling of a parabolic trough solar power plant, in: Proceedings of the 10th International Modelica Conference, 2014, pp. 409–418.
[32] A. J. Gallego, L. J. Yebra, E. Fernández Camacho, A. J. Sánchez, Mathematical Modeling of the Parabolic Trough Collector Field of the Tcp-100 Research Plant.
[33] S.J. Navas, F.R. Rubio, P. Ollero, J.M. Lemos, Optimal control applied to distributed solar collector fields with partial radiation, Sol. Energy 159 (2018) 811–819.
[34] A.J. Sánchez, A.J. Gallego, J.M. Escaño, E.F. Camacho, Temperature homogenization of a solar trough field for performance improvement, Sol. Energy 165 (2018) 1–9.
[35] W.S. McCulloch, W. Pitts, A logical calculus of the ideas immanent in nervous activity, Bull. Math. Biophys. 5 (4) (1943) 115–133.
[36] T.L. Fine, Feedforward Neural Network Methodology, Springer Science & Business Media, 2006.
[37] D.E. Rumelhart, G.E. Hinton, R.J. Williams, Learning representations by back-propagating errors, nature 323 (6088) (1986) 533–536.
[38] M.F. Møller, A scaled conjugate gradient algorithm for fast supervised learning, Neural Network. 6 (4) (1993) 525–533.
[39] A.J. Sánchez, A.J. Gallego, J.M. Escaño, E.F. Camacho, Event-based mpc for defocusing and power production of a parabolic trough plant under power limitation, Sol. Energy 174 (2018) 570–581.
[40] Solacor 2 project, URL https://solarpaces.nrel.gov/project/solacor-2 (Dec 2021).
[41] Mojave solar project, URL https://solarpaces.nrel.gov/project/mojave-solar-project (Dec 2021).